

Numerical simulations of downward convective overshooting in giants

Chun-Lin Tian,^{1,2*} Li-Cai Deng¹ and Kwing-Lam Chan³

¹National Astronomical Observatories, Chinese Academy of Sciences, Beijing 100012, China

²Graduate University of Chinese Academy of Sciences, Beijing 100049, China

³Department of Mathematics, Hong Kong University of Science and Technology, Hong Kong, China

Accepted 2009 May 30. Received 2009 May 29; in original form 2008 July 15

ABSTRACT

An attempt at understanding downward overshooting in the convective envelopes of post-main-sequence stars has been made on the basis of three-dimensional large-eddy simulations, using artificially modified OPAL opacity and taking into account radiation and ionization in the equation of state. Two types of star, an intermediate-mass star and a massive star, were considered. To avoid a long thermal relaxation time of the intermediate-mass star, we increased the stellar energy flux artificially while trying to maintain a structure close to the one given by a 1D stellar model. A parametric study of the flux factor was performed. For the massive star, no such process was necessary. Numerical results were analysed when the system reached the statistical steady state. It was shown that the penetration distance in pressure scaleheights is of the order of unity. The scaling relations between penetration distance, input flux and vertical velocity fluctuations studied by Singh et al. were checked. The anisotropy of the turbulent convection and the diffusion models of the third-order moments representing the non-local transport were also investigated. These models are dramatically affected by the velocity fields and no universal constant parameters seem to exist. The limitations of the numerical results were also discussed.

Key words: convection – hydrodynamics – turbulence – methods: numerical – stars: interiors.

1 INTRODUCTION

Turbulent convection is one of the major uncertainties in our understanding of stellar properties. As a very efficient mixing process and energy transfer mechanism, it affects the stellar structure and evolution significantly. Because of their high non-linearity and complexity, we cannot solve for turbulent flows analytically at present. Since Emden (1907) established the first practical model of stellar structure, much effort has been made to study the problem of stellar convection. A traditional treatment is the mixing-length theory (MLT; Böhm-Vitense 1958). The basic idea of MLT is that convection is viewed as rising and sinking bubbles that blend into the surroundings after travelling a distance l , where $l = \tilde{\alpha} H_p$, $\tilde{\alpha}$ is an arbitrary parameter and H_p is the local pressure scaleheight. Since the 1960s, several authors have worked directly with the hydrodynamic equations (see Spiegel 1971 and references therein). By far the most practical stellar convection theories, besides the various MLTs, are those based on the moment method (Xiong 1977, 1986, 1989a; Canuto 1993). The moment approach was introduced first by Keller & Friedmann (1924) and its first application in stellar convection was discussed by Castor (1968, unpublished, see the review by Baker 1987). In this method, the flow variables are split

into an average and a fluctuating part. Manipulation of the hydrodynamic equations based on such splitting gives a set of equations for the moments of the turbulent fluctuations. In these equations, higher order moments appear and need to be approximated by the so-called closure models. Most of these models use a gradient-type approximation, e.g. Xiong's theory. Along with the development of digital computers and computational fluid dynamics (CFD), numerical simulations have become an essential tool for the astrophysical fluid dynamic community. A pioneering work in the numerical study of stellar-type convection was the two-dimensional simulation of compressible convection by Graham (1975). Since the late 1980s, three-dimensional numerical experiments and simulations have become mainstream (Chan & Sofia 1986, 1989, 1996; Stein & Nordlund 1989; Malagoli, Cattaneo & Brummell 1990; Porter & Woodward 2000). Numerical investigations of turbulent flows fall into two categories: direct numerical simulation (DNS) and large-eddy simulation (LES). As the problem is three-dimensional, multi-length-scale and multi-time-scale, a DNS of stellar convection demands enormous computer resources. In LES, the large eddies are calculated explicitly while the smaller eddies are handled by subgrid-scale (SGS) models. This is usually the approach adopted for stellar flow simulations. The progress made by numerical simulations is usually slow, as these are limited by the speed and memory of the computers used. Even with today's machines, we still cannot simulate the whole convection zone of a post-main-sequence star

*E-mail: cltian@bao.ac.cn

directly. A frequently used approach is to make a high-resolution local simulation.

Many problems of stellar structure are associated with convective overshooting. The overshooting distance beneath an outer convection zone may affect the surface chemical composition, e.g. the depletion of lithium in the Sun. The radiative–convective boundary is thought to be closely related to the solar dynamo and is the site for magnetic flux storage. The gravity waves generated by penetration may generate momentum exchange with the interior. However, the calculation of overshooting is a challenge to all existing stellar convection theories. Owing to its intrinsic drawback, a local MLT cannot handle convective overshooting consistently. A number of non-local models have been developed to incorporate the feedback of the overshooting on the energy transport in the penetration zone, which is neglected in the local MLT. Although these models can produce overshooting, ‘they still consider convection as an extended local phenomenon’ (see Roxburgh 1998 and references therein). In Xiong’s (1985b; 1989b) hydrodynamic stellar convection theory, the difficulties caused by local treatment disappear spontaneously. Xiong’s calculations show extensive overshooting zones and the kinetic energy fluxes in such zones are negligible. At the same time, the impact on the overall stellar structure is minor (especially for zero-age-main-sequence (ZAMS) stars). However, Xiong’s closure scheme is under debate. Numerical experiments can be used to test the assumptions made in the one-dimensional (1D) models. Roxburgh & Simmons (1993) performed a two-dimensional simulation of convective penetration to study the integral constraints on the extent of overshooting by constructing a temperature-dependent radiation conductivity model. Singh, Roxburgh & Chan (1994, 1995, 1998) conducted a series of numerical experiments to examine the scaling relationships between the penetration distance (Δ_d), vertical velocity at the bottom of the convective region and total energy flux (F_b). The results of three-dimensional LESs of compressible turbulent convection were used to test the relations proposed by Schmitt, Rosner & Bohn (1984) and Zahn (1991). They confirmed $\Delta_d \propto v_{zo}^3/F_b$ for nearly adiabatic penetration and $\Delta_d \propto F_b^{1/2}$ for non-adiabatic penetration, where v_{zo} is the root-mean-square (rms) vertical velocity at the unstable–stable interface. Using the same technique, Saikia et al. (2000) found that the numerical aspects of the model, such as aspect ratio and grid number, could greatly affect the penetrative distance. Brummell, Clune & Toomre (2002) performed a large number of high-resolution, three-dimensional DNSs for the purpose of investigating the penetration and overshooting of turbulent compressible convection. In their study, the effects of rotation were included. Recently, penetration below a stellar-type rotating convection zone was estimated by Pal, Singh & Chan (2007) with a set of LESs. Rogers, Glatzmaier & Jones (2006) reported a two-dimensional simulation of gravity waves induced by overshooting below the solar convection zone. In these numerical experiments, only ideal gas with a polytropic initial distribution was considered. However, for a practical model, a realistic radiation opacity and equation of state (EOS) should be used.

According to stellar evolution theory, at the base of the giant branch in the Hertzsprung–Russell diagram convection occurs in the outer region of the envelope and extends to the deep stellar interior. When the base of the convection zone overlaps with the exhausted nuclear reaction area, turbulent convection will produce efficient mixing and dredge up the processed material to the surface of the star. This mechanism is used to explain the observed chemical peculiarities at the surfaces of certain stars. In this paper, we present a preliminary attempt to simulate overshooting below

the convective envelopes of some post-main-sequence stars. Besides the EOS and the radiation opacity (modified to accommodate an enhanced flux), the radiative pressure and radiative energy were also taken into account. In Section 2, a brief introduction to the adopted hydrodynamic code and input physics is given. The construction of the initial hydrostatic models, the simplifications and the parameters of the computational models are also specified there. In Section 3 we analyse the numerical results, with a focus on the statistical properties of the turbulent fluctuations, energy fluxes, overshooting and moment closure. A summary is given in Section 4, where the limitations and extensibility of the current study are also discussed.

2 DESCRIPTION OF THE COMPUTATIONAL MODEL

For simplicity, the magnetic field, rotation and nuclear reactions are neglected. The motion of fully ionized gas in the chemically homogeneous interior of a star is governed by the Navier–Stokes (NS) equations:

$$\partial\rho/\partial t = -\nabla\cdot\rho\mathbf{v}, \quad (1)$$

$$\partial\rho\mathbf{v}/\partial t = -\nabla\cdot\rho\mathbf{v}\mathbf{v} - \nabla p + \nabla\cdot\boldsymbol{\Sigma} + \rho\mathbf{g}, \quad (2)$$

$$\partial E/\partial t = -\nabla\cdot[(E+p)\mathbf{v} - \mathbf{v}\cdot\boldsymbol{\Sigma} + \mathbf{F}_d] + \rho\mathbf{v}\cdot\mathbf{g}, \quad (3)$$

where ρ is the density, \mathbf{v} is the velocity, p is the pressure, \mathbf{g} is the gravitational acceleration and $E = e + \rho v^2/2$ is the total energy (where e defined in equation (10) is the internal energy including ionization energy and radiation energy).

$$\boldsymbol{\Sigma} = 2\mu\boldsymbol{\sigma} + \lambda(\nabla\cdot\mathbf{v})\mathbf{I} \quad (4)$$

is the viscous stress tensor, where $\boldsymbol{\sigma}$ is the strain rate tensor, \mathbf{I} is the identity tensor and μ represents the SGS eddy viscosity:

$$\mu = \rho(c_\mu\Delta)^2(2\boldsymbol{\sigma}:\boldsymbol{\sigma})^{1/2}. \quad (5)$$

c_μ is an adjustable constant parameter, Δ is a length-scale of the order of the local grid size, and the colon represents the contraction of the tensor. The bulk viscosity λ is taken to be $-(2/3)\mu$.

$$\mathbf{F}_d = \mathbf{F}_{\text{rad}} + \mathbf{F}_{\text{sgs}} \quad (6)$$

is the diffusive flux. \mathbf{F}_{rad} is the radiative flux, which can be accurately computed as diffusion in the deep interior of the star, i.e.

$$\mathbf{F}_{\text{rad}} = -\frac{4acT^3}{3\kappa\rho}\nabla T. \quad (7)$$

a is the radiation density constant, c is the speed of light and κ is the Rosseland mean opacity.

$$\mathbf{F}_{\text{sgs}} = -\frac{\mu}{\sigma_{\text{sgs}}}C_p\left(\nabla T - \nabla_a\frac{T}{p}\nabla p\right) \quad (8)$$

stands for the diffusive energy transport by SGS turbulence. σ_{sgs} is the effective Prandtl number for the SGS model (hereafter, σ_{sgs} is called the SGS Prandtl number), C_p is the specific heat of the gas at constant pressure and ∇_a is the adiabatic gradient.

The SGS Prandtl number σ_{sgs} is taken to be 1/3; the Deardorff number c_μ in equation (5) is fixed at 0.2. Near the solid boundaries, the SGS viscosity is enhanced to absorb irrelevant acoustic waves. In the stable region, the turbulent diffusive flux (8) is taken to be zero. The equations (1)–(3) are solved in Cartesian coordinates (x, y, z) , where $z = (r - r_b)/d$ for r (radius) $\in [r_b, r_b + d]$. r_b and d are the radial location of the bottom and the height of the computational domain, respectively (see Section 2.3). The computed domain

is a rectangular box with periodic boundaries on the sides and solid boundaries at the top ($z = 1$) and bottom ($z = 0$). The aspect ratio of the domain (width/height) is 1.5. The total energy flux F_b is fixed at the bottom; at the top the entropy is fixed. The grid distribution is horizontally uniform. In the vertical direction, the grid spacing decreases smoothly with the height. All cases use a $64 \times 64 \times 96$ mesh.

2.1 Numerical scheme: ADISM

We adopted the ADISM (Alternating Direction Implicit method on Staggered Mesh) scheme of Chan & Wolff (1982) to solve the full NS equations (1)–(3). This method has second-order accuracy in space, which is adequate for simulating the turbulent situation. As an implicit scheme, it can avoid the time-step restriction imposed by sound waves associated with the Courant–Friedrichs–Lewy (CFL) condition (see Richtmyer & Morton 1968). Numerical tests show that the ADISM scheme can maintain stability for a time-step over 100 times the normal value suitable for explicit schemes. In contrast with most other implicit methods, the CPU time consumption of the ADI method is linearly proportional to the number of grid points. A detailed examination of the ADISM approach has been given by Chan & Sofia (1986). The hydrodynamic code we used was initially developed and used by Chan & Sofia (1989) and then adopted by Kim & Chan (1998) to study the upper solar transition layer. Therefore, it has been well debugged.

2.2 Input physics: EOS and opacity

In the simulated region, the temperature is high enough that all kinds of atoms are fully ionized. For a density ρ and a gas particle mass Am_H , the Coulomb energy per particle is $e_C = \tilde{Z}^2 e^2 / (4\pi\epsilon_0 \mathcal{D})$, where $\tilde{Z}e$ is the particle charge, ϵ_0 is the permittivity, $\mathcal{D} = (Am_H/\rho)^{1/3}$ is the mean interparticle distance and m_H is the atomic mass unit. At temperature T , the kinetic energy per particle has the form $e_k = 3kT/2$, where k is the Boltzmann constant. The ratio of Coulomb energy to kinetic energy can be estimated as

$$\frac{e_C}{e_k} = \left[\frac{\tilde{Z}^2 e^2}{6\pi\epsilon_0 k (Am_H)^{1/3}} \right] \frac{\rho^{1/3}}{T}, \quad (9)$$

where A and \tilde{Z} are of the order of unity, and the term in square brackets is approximately 10^5 . For our modelled cases, the ratio of $\rho^{1/3}/T$ is less than $10^{-6.5}$, which means $e_C/e_k \approx 0.01$. This indicates that the particle interactions are dominated by collisions and the non-ideal effects caused by the Coulomb force can be safely neglected. Hence, for the present calculation, the gas is treated as a fully ionized ideal gas. The internal energy e and total pressure p can be expressed as

$$e = aT^4 + \frac{3}{2}p_g + \rho e_i, \quad p = p_g + p_r, \quad (10)$$

respectively, where $p_g = \beta p$ is the gas pressure, p_r is the radiation pressure and e_i is the ionization energy per mass unit. Using equations (10) we can conveniently calculate thermodynamic variables such as C_p , ∇_a , $(\partial T/\partial \rho)_e$, etc. Comparisons show that the discrepancies between the ρ , C_p and ∇_a calculated by equation (10) and the interpolation from the OPAL EOS tables (Rogers, Swenson & Iglesias 1996) are less than 2 per cent in the regions we computed.

The opacity κ is obtained by interpolating the OPAL tables (Rogers & Iglesias 1992). Before interpolation, the OPAL opacity is tabulated as a function of density and $\mathcal{R} = \rho/(T \times 10^{-6})^3$

Table 1. Key properties of the reference stars.

M/M_\odot	$\log(T_e)$	$\log(L/L_\odot)$	Age (yr)	R/R_\odot
3	3.695	2.032	4.258×10^8	14.113
15	3.761	4.869	1.308×10^7	273.376

Both of these stars have the same chemical composition : $X = 0.7$, $Z = 0.02$.

in two-dimensional arrays with even $\Delta \ln \rho$ and $\Delta \ln \mathcal{R}$. A *hunt* method is used to search the table.

2.3 Initial models: construction and modifications

We consider two types of post-main-sequence star: a massive star of $15 M_\odot$ (red supergiant) and an intermediate-mass star of $3 M_\odot$ (red giant). The regions we study are far away from the core and surface, so that we need not consider the non-local thermal equilibrium (LTE) effects and nuclear reactions. Our 1D reference stellar models are computed with more realistic input physics and Xiong's non-local time-dependent stellar turbulent convection theory (private communication). The model properties (i.e. mass M , effective temperature T_e , luminosity L , age and radius R) are listed in Table 1.

In the simulation of the intermediate-mass star envelope, we have encountered serious difficulties. They are discussed as follows.

(i) The first problem is the very long duration of thermal relaxation. The thermal relaxation time-scale can be estimated by dividing the total energy contained in the system by the rate of energy input at the bottom. For an intermediate-mass star, the dimensionless input energy flux (F_b) is of the order of 10^{-5} and the radial integral of energy density energy (e) above the bottom ($z = 0$) is of the order of 1000. This means that the system needs a time-scale of 10^8 to reach a thermally relaxed state. The time-step achieved by the ADISM scheme is around 10^{-2} for the current study. Therefore, we need about 10^{10} steps to accomplish the relaxation. This requires too many computational resources.

(ii) Meanwhile, the limited spatial resolution is unable to handle the small superadiabatic gradient ($\Delta \nabla = \partial \ln T / \partial \ln p - \nabla_a$) accurately. In the efficient convective region, $\Delta \nabla$ is of the order of 10^{-6} , which would be easily overwhelmed by the numerical truncation errors.

A way to work around the above problems is to enlarge the total energy flux (and thus the superadiabatic gradient) to make the computation feasible. The stellar thermal structure and convective stability are mainly determined by the energy transport mechanism and the superadiabatic gradient. Using the expression for the diffusive radiative flux, we have

$$\frac{dT}{dz} = -\frac{3\kappa\rho F_{\text{rad}}}{4acT^3}, \quad (11)$$

$$\frac{dp}{dz} = \frac{p}{(\Delta \nabla + \nabla_a)T} \frac{dT}{dz} = \rho g, \quad (12)$$

where

$$\nabla_a = \nabla_a(p, T), \quad (13)$$

$$\kappa = \kappa(p, T), \quad (14)$$

$$\rho = \rho(p, T). \quad (15)$$

Given the distributions of F_{rad} and $\Delta\nabla$, the EOS and opacity and the values of p , T at one boundary, we can integrate (11) and (12) to construct a stratified layer of fluid close to the reference stellar model.

In order to reduce the thermal relaxation time for the intermediate-mass star model, the radiative flux F_{rad} ($=F_{\text{b}}$ in the radiative region) must be enlarged dramatically (by a factor of $a_f \gg 1$). This would make the thermal structure calculated by equations (11) and (12) totally different from the reference stellar structure. This problem can be solved by dividing the opacity by the same factor a_f . In doing so, P , T and the profile of $F_{\text{rad}}/F_{\text{b}}$ are similar to the reference stellar model and only the magnitude of F_{rad} is enhanced. In the interior of stars, for constant luminosity, F_{rad} is inversely proportional to the square of radius r . If the structures calculated in spherical coordinates are into the Cartesian frame, the systems will undergo large adjustments and will substantially deviate from the initial 1D stellar models. The radiation conductivity is multiplied by a factor $c_r = (r_b + z)^2/r_b^2$ to avoid such adjustment. Here r_b is the distance from the bottom of the computed domain to the stellar centre. Hence, for the calculations, we use an effective opacity $\kappa^* = \kappa/(c_r a_f)$ instead of the real κ .

An initial stratified layer constructed by the above method is specified by the six parameters ρ_t , p_t , T_t , a_f , r_b and d (the subscript ‘t’ denotes values at the top), and two distributions: F_{rad} and $\Delta\nabla$. Their values are chosen to make the initial state close to the reference model.

In the interior of the massive star, convection is not very efficient. The zone extends for about 3.41 pressure scaleheights (PSHs) (0.25 of the stellar radius R). The upper convective boundary is located in the deep interior. The typical value of $\Delta\nabla$ is of the order of 0.001 in the convection zone, and about -0.06 in the stable region below. The computed domain of our massive star model contains about 6.8 PSHs ($d = 0.379R$) in total. It includes the whole convection zone and a lower stable layer. The upper boundary is a little higher than the actual top of the convection zone of the 1D reference model. The distance between the bottom of the computed domain and the centre of the star is $r_b = 0.379R$. The initial distributions of the radiative flux F_{rad} and superadiabatic gradient $\Delta\nabla$ for the various models are shown in Fig. 1 by dotted lines without amplification factors (e.g. $a_f = 1$). The other characteristics of the initial models are given in Table 2.

For the massive star, the values of F_{btm} and other quantities are computationally manageable and a_f can be chosen to be 1. On the other hand, the parameters of the convection zone of the intermediate-mass star have to be modified to make the calculations feasible. We use several values of a_f to check for the parametric behaviour of the modified models. The convection in the red giant extends to a height of about 14 PSHs ($0.4R$). A direct simulation of such a deep layer is unaffordable even with an enlarged energy flux. We can only consider the lower part of the convection zone. The computed box has a shorter radial extension ($d = 0.1R$) and the top is placed at the middle of the convection zone. r_b is at $0.6R$. Consequently, the unstable layer is about 2.7 PSHs thick and the whole computed domain contains about 6.6 PSHs. To suppress the significant thermal adjustment caused by truncating the convection zone, an artificial thermal control layer is introduced near the upper boundary. This is a slightly subadiabatic layer with an artificial conductivity set to $-F_{\text{rad}}/(dT/dz)$ so that radiation carries all of the energy flux. The corresponding layer is indicated by the dashed line in Fig. 1.

The dimensionless input energy flux (F_{btm}) for the intermediate-mass star model is very small (see the last column in Table 2). To

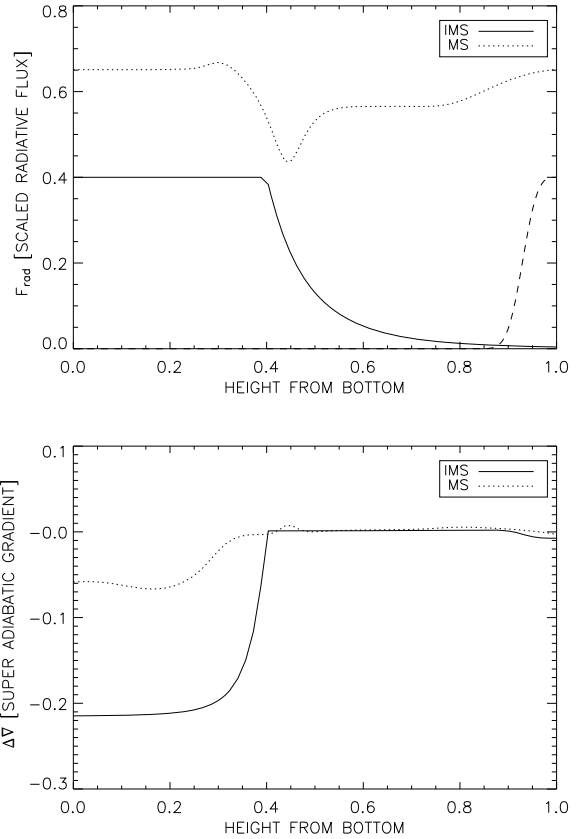


Figure 1. Initial distributions of radiative flux and superadiabatic gradient for an intermediate-mass star (IMS) model (solid lines) and a massive star (MS) model (dotted lines). The MS model is taken from a 1D stellar model and the IMS model is constructed according to the 1D stellar model. Cases I1, I2 and I3 listed in Table 3 have the same initial $\Delta\nabla$ and different initial F_{rad} . The solid line in the upper panel is an example of the initial distribution of F_{rad} for the IMS model ($2 \times F_{\text{rad}}$ of Case I3). The dashed line is the fake stable layer introduced to prevent dramatic effects near the upper boundary. The abscissa is the height from the bottom $z = (r - r_b)/d$ for $r \in [r_b, r_b + d]$, where d is the height of the computed zone and r_b is the location of the bottom.

reduce the thermal relaxation time, several values of a_f around 10^4 are used. In constructing the initial model, the flux and geometry were modified through the controlling parameters a_f , c_r , d and r_b . Among the modifications, we care most about the effects caused by a_f . Three intermediate-mass star models are constructed with different values of a_f (see Table 3). If a_f is much greater than in Case I3, the program can easily crash, and a value smaller than that in Case I1 would cause the results to be affected by numerical errors (truncation and round-off errors). In Table 3, F_{b} is the modified dimensionless numerical input energy flux, i.e. $F_{\text{b}} = F_{\text{btm}} c_r a_f$. The initial superadiabatic gradient and radiation flux for the intermediate-mass star models are shown in Fig. 1. The three models have the same initial $\Delta\nabla$ (see the solid line in the bottom panel of Fig. 1). Their F_{rad} curves have the same shape but different magnitudes: the top panel of Fig. 1 simply gives an example of radiation flux distribution. Twice the initial F_{rad} of Case I3 is plotted for clarity. Note that the constructed intermediate-mass star models are based on local convection theory, i.e. there is no overshoot hump in the radiative flux distribution (compare with fig. 5 of Xiong & Deng 2001, hereafter XD2001).

Table 2. Definition of the physical model.

Type of star	$\log(p_{\text{scl}})$	$\log(T_{\text{scl}})$	$\log(\rho_{\text{scl}})$	p_{btm}	T_{btm}	ρ_{btm}	d/R	r_b/d	F_{btm}
Intermediate	7.881	4.872	-5.116	737.152	6.226	118.276	0.1	6	0.2×10^{-4}
Massive	5.820	5.022	-7.602	927.728	5.095	226.088	0.379	1	0.651

$p_{\text{btm}}, T_{\text{btm}}, \rho_{\text{btm}}$ are scaled by $p_{\text{scl}}, T_{\text{scl}}, \rho_{\text{scl}}$ respectively. The input flux $F_{\text{btm}} = F_b/(c_T a_f)$ is scaled by $(p_{\text{scl}}^{1.5}/d_{\text{scl}}^{0.5})$, where F_b is the modified dimensionless input flux.

Table 3. Characteristics of the numerical runs.

Identifier	a_f	F_b	t	σ_{max} (per cent)
I1	1×10^4	0.05	9295	5.9
I2	2×10^4	0.10	7316	1.7
I3	4×10^4	0.20	5844	1.3
M1	1.0	0.651	11298	1.8

a_f, F_b, t and σ_{max} are the amplifying parameter, dimensionless input energy flux, dimensionless relaxation time and maximum deviation of the average total energy flux from the input flux, respectively.

For convenience, we make all the quantities dimensionless by scaling the variables so that ρ_t, p_t, T_t and d all have the value unity. The scalings $\rho_{\text{scl}}, p_{\text{scl}}$ and T_{scl} are given in Table 2. d/R represents the radial fraction of the domain included in the computation, and the last column gives the dimensionless energy fluxes of the unmodified models. All the scalings of the other variables can be deduced from dimensional analysis.

3 RESULTS AND DISCUSSION

After a long period of thermal relaxation, the flow reaches a statistically steady state and its average properties become stationary. One criterion of thermal relaxation is that the input energy flux from the bottom is balanced by the outgoing energy flux through the top surface. In the present calculations, the deviations of the averaged vertical total flux from the input energy flux are less than 2 per cent everywhere (except Case I1, which has a bound of 6 per cent). The maximum discrepancies occur near the unstable–stable interfaces (where the cross-correlation of temperature and vertical velocity changes its sign).

In expressing the results, the overline denotes a combination of horizontal and temporal averaging, the prime (′) denotes the deviation from the mean, and the double prime (′′) denotes the rms fluctuation from the mean. In some of the figures, the locations of integral pressure scaleheights counted from the upper boundary are also shown. For example, in Fig. 2 the first vertical dashed line from the right is 1 PSH away from the top boundary. $H_p = -dr/d \ln p$ sometimes does not increase monotonically with depth, as the gravity g is variable and the EOS has a complex form. In some plots (e.g. Fig. 2), the overshooting zone Δ_c , defined in Section 3.4, is indicated by a double-headed arrow.

3.1 Stationary solutions

Fig. 2 shows the distributions of averaged vertical fluxes for Cases I2 and M1, from which we can see that the systems are almost completely relaxed. The different energy fluxes are defined as follows:

$$F_e = \overline{v_z(e + p)} \quad (16)$$

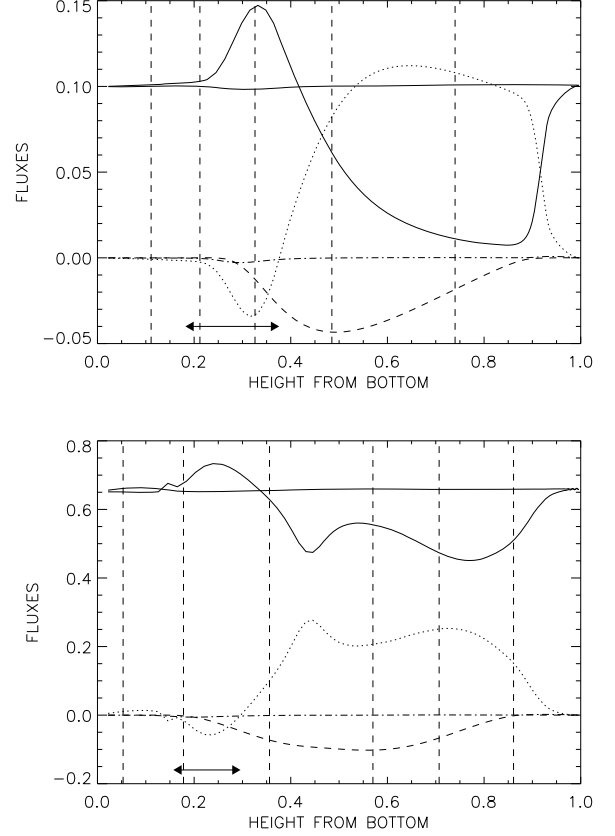


Figure 2. Height distributions of average fluxes for Cases I2 (top) and M1 (bottom). The enthalpy flux, kinetic flux, viscous flux, diffusive flux and total flux are represented by dotted lines, dashed lines, dot–dashed lines, dot–dot–dashed lines and solid lines, respectively. The double-headed arrow indicates the overshooting zone, defined by negative convective flux. The vertical dashed lines represent the integral pressure scaleheights counted from the upper boundary.

is the enthalpy flux,

$$F_k = \frac{1}{2} \overline{v_z \rho v^2} \quad (17)$$

is the flux of kinetic energy and

$$F_v = \overline{v_i \Sigma_{iz}} \quad (18)$$

is the small-scale eddy viscosity flux, where the Einstein summation convention is used. The diffusive flux F_d is defined in (6) and the total flux is $F_t = F_e + F_k + F_v + F_d$. A more detailed discussion of these fluxes is given in Section 3.3.

As an important indicator of convective instability, the superadiabatic gradient $\Delta \nabla$ is given in Fig. 3 for all the cases. Here we focus on Cases I1–I3. Highly superadiabatic regions occur near the upper stable–unstable interfaces, where the systems are substantially unstable. The sharp jumps may be caused by the lack of enough room for upward motions. The same phenomenon was found in

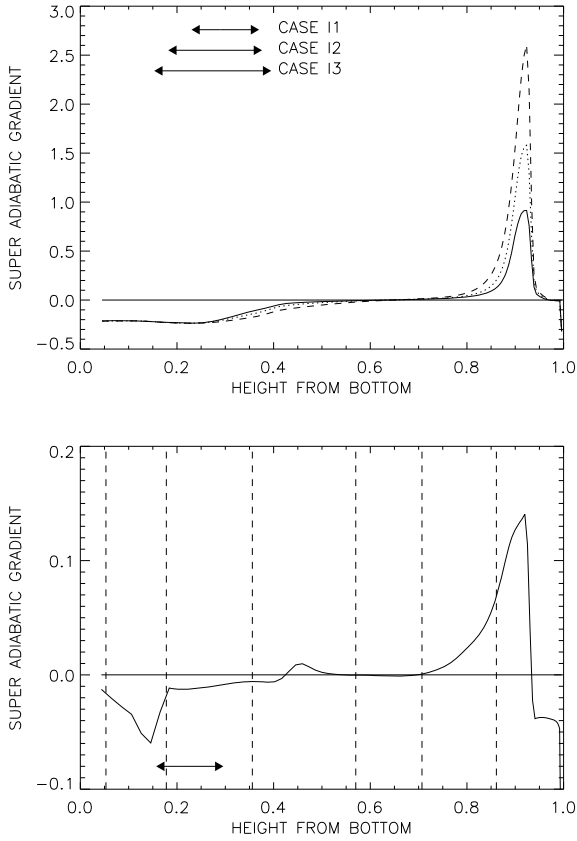


Figure 3. Height distribution of the superadiabatic gradient for Cases I1–I3 (top) and M1 (bottom). In the top panel, the solid line represents I1, the dotted line I2 and the dashed line I3. The double-headed arrow indicates the overshooting zone. The vertical dashed lines represent the integral pressure scaleheights counted from the upper boundary. The very large superadiabatic gradients near the upper boundary are mainly caused by the solid boundary conditions. In the middle region of the convection zone, the small superadiabatic gradient could be affected by the numerical errors (see text for details).

Singh, Roxburgh & Chan (1998)’s work (see fig. 5 therein). In the convection zone, $\Delta\nabla$ is not as small as in the 1D reference model. This is caused by the enhanced total flux. The slightly negative $\Delta\nabla$ in the lower part of the convection zone ($0.4 < z < 0.6$) indicates that $\Delta\nabla$ is sensitive to even small numerical inaccuracies. A higher order scheme with a denser mesh may eliminate such problems.

Fig. 4 shows examples of the velocity fields projected on to a vertical plane. We can see from these figures that the turbulent flows are dominated by large eddies, the sizes of which are comparable to at least a pressure scaleheight. The small-scale flows are mostly associated with downward plumes. The penetrations of such plumes into the overshoot zone are also shown. The upper solid lines in Fig. 4 (near $z = 0.4$ for Case I2, and $z = 0.3$ for Case M1) show the convective boundary where the enthalpy fluxes change sign. The regions between two horizontal solid lines are the overshooting zones, with depths Δ_c defined in Section 3.4. In the lower stable layer, the motions are mainly horizontal. This is characteristic of flows in convectively stable regions.

3.2 Fluctuations

Two examples (Case I2 and Case M1) of the relative fluctuations of the thermodynamical variables are shown in Fig. 5, where

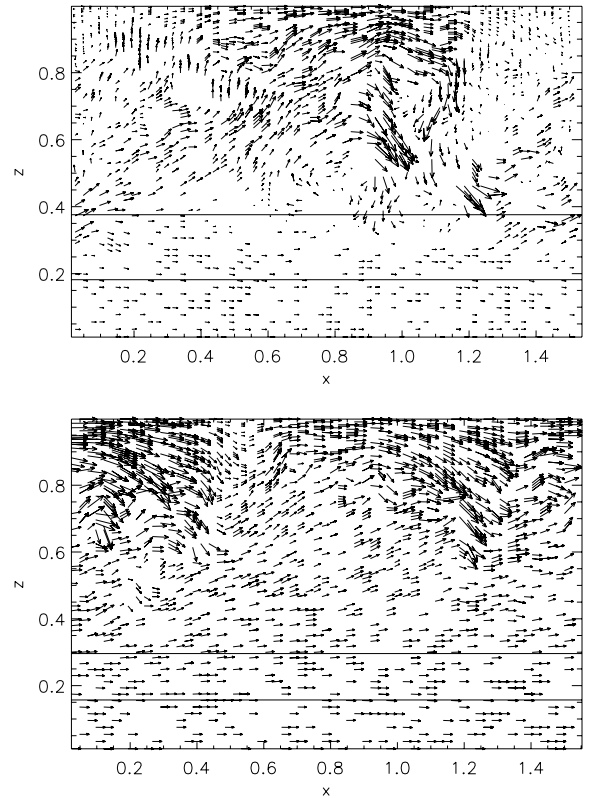


Figure 4. Velocity field projected on to the x - z plane at $y = 0.75$. Upper panel: Case I2; lower panel: Case M1. The regions confined by solid lines indicate the overshooting zones, i.e. Δ_c defined in Section 3.4.

$\rho''/\bar{\rho}$, p''/\bar{p} and T''/\bar{T} are represented by the solid, dotted and dashed lines, respectively. In the intermediate-mass star models, the relative fluctuation of temperature is comparable to that of density. In the overshooting region, the temperature fluctuation shows a hump. In the massive star model where convection is inefficient, T''/\bar{T} is substantially smaller than $\rho''/\bar{\rho}$. Compared with $\rho''/\bar{\rho}$ and T''/\bar{T} , the distribution of p''/\bar{p} is relatively smooth.

The scaling relationships between the relative fluctuations and the input energy fluxes are of particular interest. Fig. 6 illustrates them for our models. The relative fluctuations of thermodynamical variables are scaled by $F_b^{0.5}$. Fig. 7 illustrates the scaling relations between the velocity fluctuations and the input flux. The velocity fluctuations are scaled by $F_b^{0.25}$. Away from the lower overshooting region, these kinds of scaling relationships are good. Only Case I3 shows some small shifts in the curves. In this case turbulent convection is not as efficient as in Cases I1 and I2. In the overshooting region, the vertical velocity fluctuations prefer the scaling $v_z'' \propto F_b^{1/3}$. The reason why the current scaling relationships (e.g. $v_z'' \propto F_b^{0.25}$) are different from those of Chan & Sofia (1989, hereafter CS89) (e.g. $v_z'' \propto F_b^{1/3}$) is primarily the influence of radiation. Convection in the current models is not as efficient as in CS89. Radiation diffusion plays a very significant role even in the convection zone.

3.3 Fluxes

As illustrated in Fig. 2, different mechanisms dominate the energy transport in different regions of the computed models. In the stable regions, the energy is predominantly transported by radiation. Enthalpy flux and kinetic flux are the dominant modes of energy

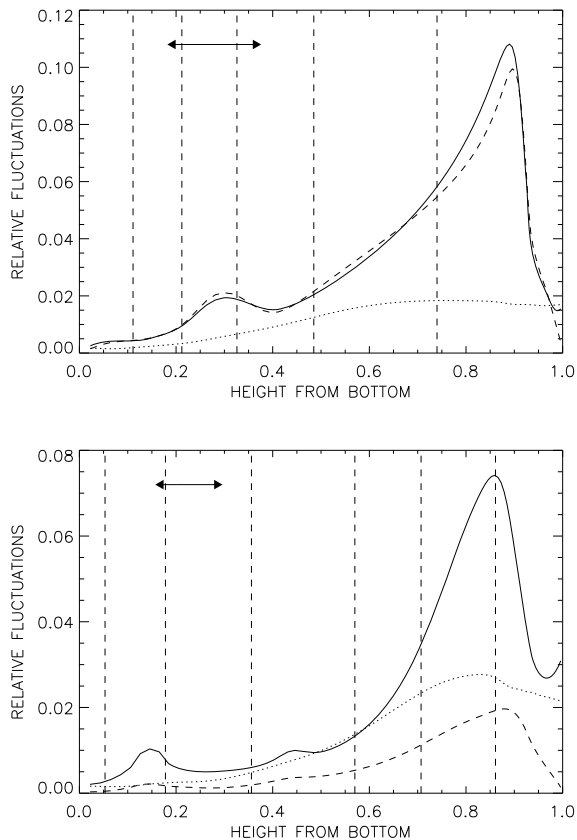


Figure 5. Height distributions of relative fluctuations of density, pressure and temperature for Cases I2 (upper panel) and M1 (lower panel). Solid lines: $\rho''/\bar{\rho}$; dotted lines: p''/\bar{p} ; dashed lines: T''/\bar{T} . The double-headed arrow indicates the overshooting zone. The vertical dashed lines represent the integral pressure scaleheights counted from the upper boundary.

transport in the convection zones. In the overshooting layer, energy transport is amidst the counterbalance of convection and radiation. The hump in the distribution of radiative flux is to balance the negative enthalpy flux in the overshooting layer. The relative amplitudes of these humps are about five times those based on Xiong's theory (see fig. 5 in XD2001). This may simply reflect the fact that the total energy flux has been artificially enhanced.

Fig. 8 compares the different types of energy fluxes scaled by the powers of input flux. Unlike the results of CS89, F_e and F_k are not scaled by F_b here. The kinetic fluxes are approximately scaled by $F_b^{0.75}$, which could be regarded as a consequence of $v_z' \propto F_b^{0.25}$, since $F_k \propto v_z' v''^2 \propto v_z'^3$ where $v''^2 = v_x''^2 + v_y''^2 + v_z''^2$. Fig. 8(c) shows that in the convection zones F_d is not scaled by F_b . This is also a consequence of significant effects of radiation. High non-linearity makes the analysis of such a phenomenon very difficult.

Since F_{rad} is amplified by a factor of $a_f \sim \mathcal{O}(10^4)$, the flux parameter is far from the correct value. Although we have constructed three cases with different a_f to check for the scalings, the results are restricted by the limited range of values accessible by numerical simulations. The extent of the computed domain and the boundary conditions can also affect the relationships. All these make the applicability of the scaling relations debatable. A comprehensive investigation of these uncertainties needs a large number of models and massive computations. It is beyond the scope of the present study.

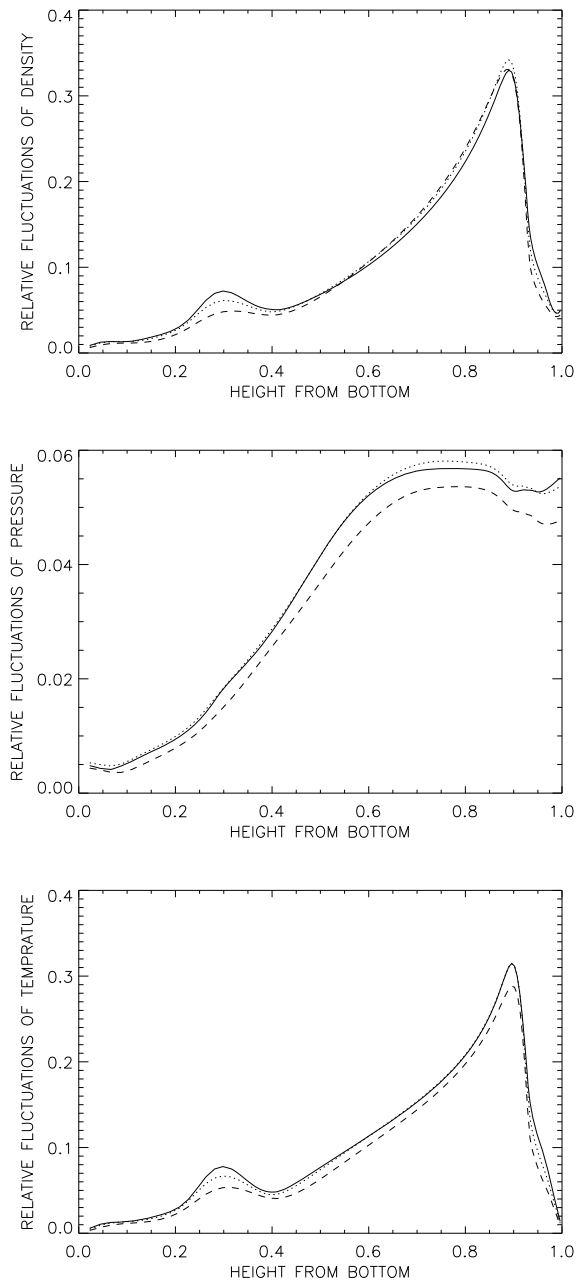


Figure 6. Comparison of scaled fluctuations of thermodynamic variables, i.e. $\rho''/(\bar{\rho}F_b^{0.5})$, $p''/(\bar{p}F_b^{0.5})$ and $T''/(\bar{T}F_b^{0.5})$. Solid lines: Case I1; dotted lines: Case I2; dashed lines: Case I3.

3.4 Overshooting

Ideally, the overshooting Δ_d is measured by the distance from the instability boundary ($\Delta\nabla = 0$) to the place where the transport velocity vanishes ($v_z = 0$). In reality, due to the various numerical limitations, this is impractical. Following Singh et al. (1995), we define Δ_d to be the location at which F_k falls to 5 per cent of its value at the stable–unstable interface. An alternative choice has been suggested by Deng & Xiong (2008). They argued that the overshooting distance should be defined as the depth of the region where the convective enthalpy flux is negative. We also consider this length and denote it by Δ_c . Numerical estimates of the overshooting distances are listed in Table 4.

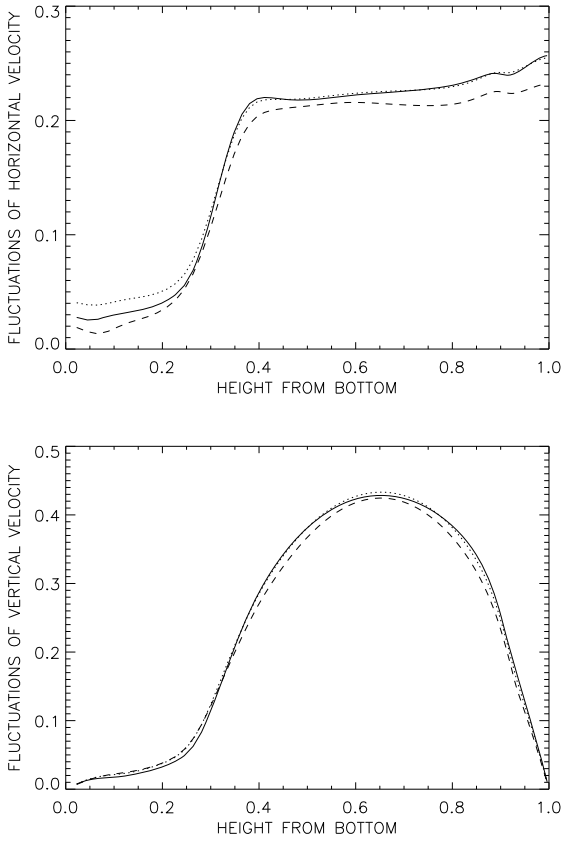


Figure 7. Comparison of scaled fluctuations of $v'_x(v'_x/F_b^{0.25})$ and $v'_z(v'_z/F_b^{0.25})$. Solid lines: Case I1; dotted lines: Case I2; dashed lines: Case I3.

As we mentioned earlier, in thermally relaxed systems there is no extensive adiabatic layer. For each of the cases, a thin layer with highly superadiabatic stratification exists near the upper unstable–stable interface. $\Delta\nabla$ changes its sign in the middle of the computed domain but remains close to zero until the lower unstable–stable interface of the initial model is reached. $\Delta\nabla$ then becomes substantially negative (see Fig. 3). Therefore, we measure Δ_d as the distance between the *initial* unstable–stable interface and the location where F_k has fallen to 5 per cent of its value at the initial stable–unstable interface. Similarly, the vertical velocity fluctuation at the convective boundary, v'_{zo} , is calculated at the initial unstable–stable interface. The upper boundary of Δ_c is the convective boundary where the enthalpy flux changes its sign. For Case M1, the lower boundary of Δ_c is at the place where F_e changes its sign again. For Cases I1–I3, it is at the layer where $|F_e| = 5$ per cent of $|\min(F_e)|$. Since Δ_d is substantially less than Δ_c and is affected by the vertical resolution, we study the scaling relationships between Δ_c , v'_{zo} and F_b instead of Δ_d , v'_{zo} and F_b .

The overshoot extents from the present study are comparable to the local pressure scaleheights and well scaled by $v'^{3/2}_{zo}$. The scaling relationship between Δ_c and $F_b^{1/2}$ is acceptable except for Case I3. This may be due to the more serious influence of radiation diffusion in I3 (the Peclet number gets smaller). From the last two columns of Table 4, one may infer a scaling $v'_{zo} \propto F_b^{1/3}$, which is not consistent with $v'_z \propto F_b^{0.25}$ given in Section 3.2. In fact, $v'_z \propto F_b^{1/3}$ works better than $v'_z \propto F_b^{0.25}$ in the lower overshooting zone. If we use the scaling relation $\Delta \propto F_b^{1/2}$ to calculate the overshooting distance for $a_f = 1$, the resulting value will be very small. However, the last column

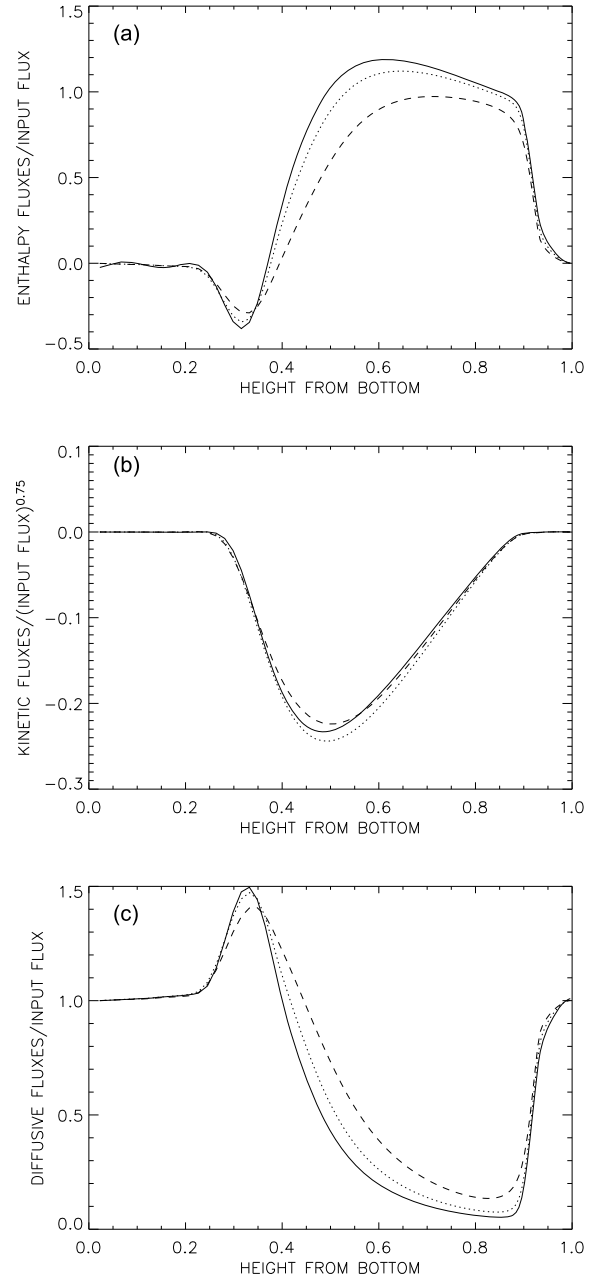


Figure 8. Comparison of scaled fluxes for an intermediate-mass star model. (a) F_e/F_b ; (b) $F_k/F_b^{0.75}$; (c) F_d/F_b . Solid lines: Case I1; dotted lines: Case I2; dashed lines: Case I3.

Table 4. The overshooting distance and its scaling relationships.

Model	Δ_d (in PSHs)	Δ_c (in PSHs)	$\Delta_c/v'^{3/2}_{zo}$	$\Delta_c/F_b^{1/2}$
I1	0.120 (0.910)	0.140 (1.117)	2.731	0.626
I2	0.124 (0.956)	0.194 (1.658)	2.952	0.614
I3	0.128 (0.993)	0.241 (2.058)	3.065	0.541
M1	0.224 (1.674)	0.139 (0.856)	2.374	0.173

PSHs stands for pressure scaleheights. v'_{zo} is the vertical velocity fluctuation at the initial stable–unstable interface. All of these are dimensionless values.

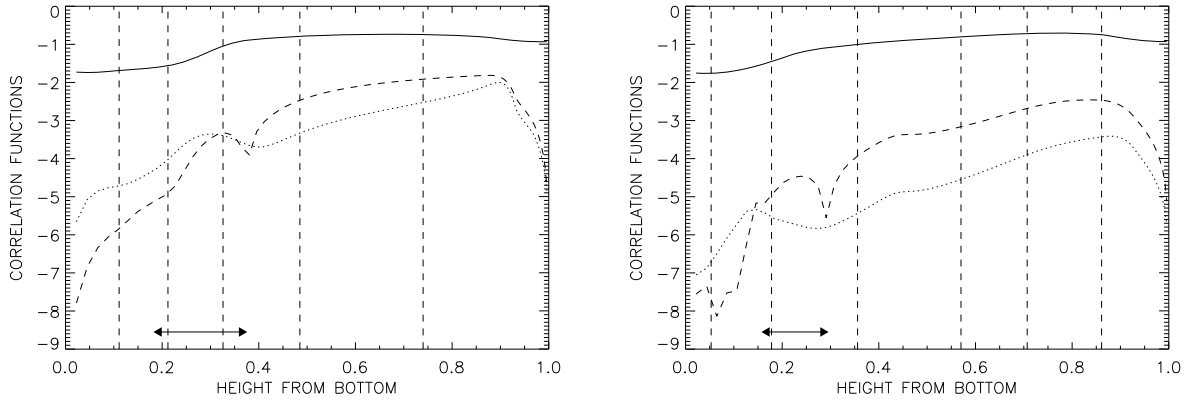


Figure 9. Common logarithms of χ (solid lines), \mathcal{Z} (dotted lines) and $|\mathcal{V}|$ (dashed lines) for an intermediate-mass star model (Case I2, left panel) and a massive star model (Case M1, right panel). The double-headed arrow indicates the overshooting zone.

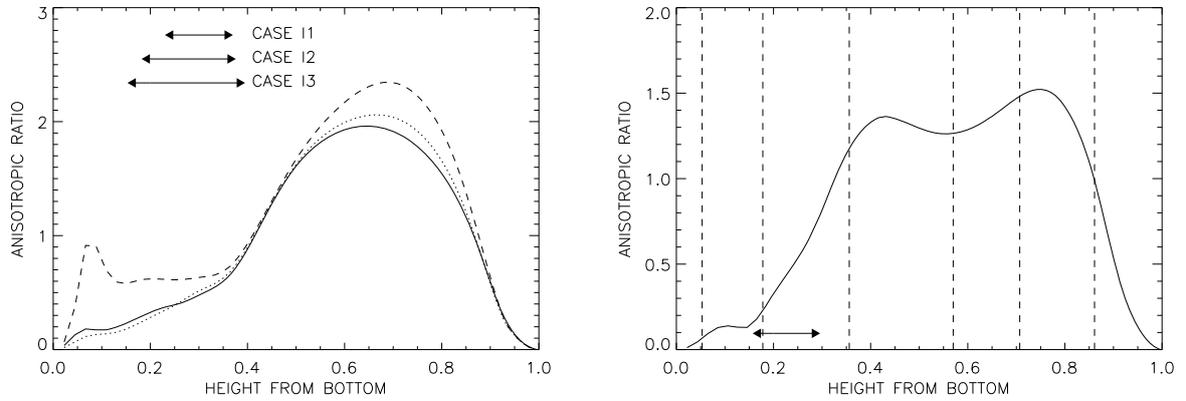


Figure 10. Height distributions of the anisotropic ratio $w_z''^2/(w_x''^2 + w_y''^2)$ of intermediate-mass star models (left panel – solid line: Case I1; dotted line: Case I2, dashed line: Case I3) and a massive star model (Case M1, right panel). The double-headed arrow indicates the overshooting zone.

of Table 4 shows that the ratio $\Delta_c/F_b^{1/2}$ increases as F_b decreases. Consequently, it is possible that the overshooting distance is still substantial when F_b is close to the realistic value. The penetration distance for Case M1 is a direct simulation without scaling. It is comparable to the value of 0.63 obtained by Xiong’s convection model (XD2001).

Numerical simulations and Xiong’s 1D stellar convection theory generally give overshoot extents comparable to the local H_p . However, helioseismological inferences give a small overshoot extent, e.g. $\sim 0.1H_p$ (Basu, Antia & Narasimha 1994). As pointed out in XD2001, the discrepancy may be caused by the assumption of a break in the radial derivative of the sound speed. The break is a consequence of the local MLT and does not appear in Xiong’s theory.

3.5 Anisotropic turbulence

Xiong’s (1977, 1989a) non-local time-dependent stellar convection theory is a dynamical theory of auto- and cross-correlation functions of the turbulent velocity and temperature fluctuations. These fluctuations are defined as derivations from the density-weighted averages, namely

$$u'_i = v_i - \frac{\rho v_i}{\bar{\rho}}, \quad \tilde{T}' = T - \frac{\rho T}{\bar{\rho}}. \quad (19)$$

The starting point of Xiong’s theory is a set of partial differential equations for $\chi^2 = \overline{w'_i w'^i}/3$, $\mathcal{Z} = \overline{\tilde{T}'^2}/\tilde{T}^2$ and $\mathcal{V} = \overline{\tilde{T}' w'_i}/\tilde{T}$,

where $w'_i = \rho u'_i/\bar{\rho}$, $\tilde{T} = \overline{\rho T}/\bar{\rho}$ and the summation convention for repeated indices is used. The closure model contains three adjustable parameters, c_1 , c_2 and c_3 , which describe the turbulent dissipation, non-local turbulent diffusion and anisotropy, respectively. Deng, Xiong & Chan (2006) stated that in the convectively unstable region, the ratio of the vertical component to the horizontal component of motion is $w_z''^2/(w_x''^2 + w_y''^2) = (3 + c_3)/2c_3$. In the upper overshooting zone, $w_z''^2/(w_x''^2 + w_y''^2) \sim 0.5$, which is independent of c_3 . In the lower overshooting zone, $w_z''^2/(w_x''^2 + w_y''^2) \leq 0.5$ and it increases with c_3 .

The common logarithms of χ , \mathcal{Z} and $|\mathcal{V}|$ for the model cases are given in Fig. 9. In both plots, $\log \mathcal{Z}$ is the smallest one within the unstable zone, and it becomes greater than $|\mathcal{V}|$ in the lower overshooting layer. The downward dip of the dashed lines near the bottom of the convective layer indicates the sign change of \mathcal{V} at the convective boundary. The distributions of $w_z''^2/(w_x''^2 + w_y''^2)$ for different models are given in Fig. 10. Tian et al. (2009, hereafter TDXC) and the current simulations suggest that the spatial distribution of the anisotropic ratio $w_z''^2/(w_x''^2 + w_y''^2)$ is very sensitive to the characteristics of the model. The maximum value generally occurs inside the convection zone. From Fig. 10 of the current study and fig. 6 of TDXC, we can see that the maximum value of the anisotropic ratio varies between 1.8 and 2.8. Cases I1–I3 show that a larger input flux creates a larger anisotropic ratio. For Case M1, in which only a fraction of the total energy flux is carried by convection, the maximum anisotropic ratio is about 1.5. Since $w_z''^2/(w_x''^2 + w_y''^2) = (3 + c_3)/2c_3$ holds only in the fully

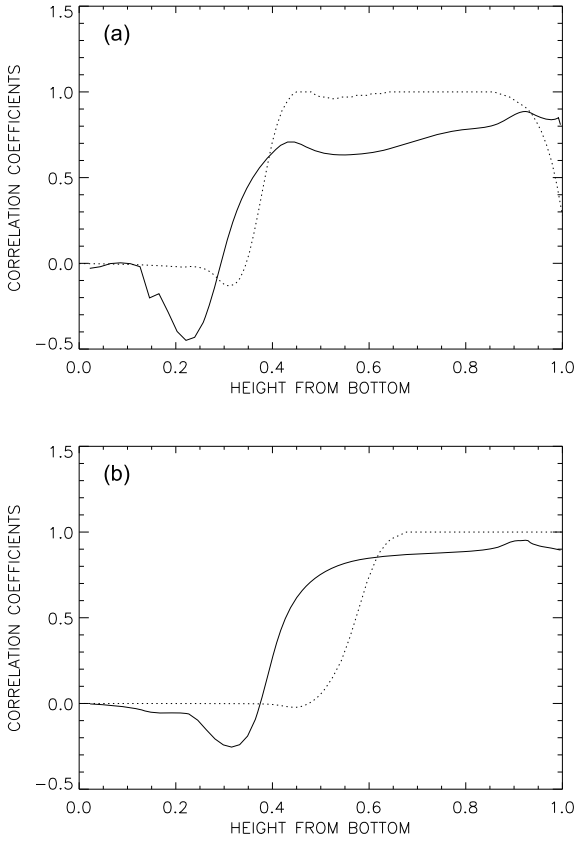


Figure 11. Comparison of the correlation coefficients of temperature and velocity, i.e. $\mathcal{V}/(\chi_z \mathcal{Z})^{0.5}$. (a) Massive star model; (b) intermediate-mass star model. Solid lines: numerical results; dotted lines: data from the 1D stellar model based on Xiong’s convection theory. Note that in panel (b), the abscissae of the solid and dotted lines are scaled with different lengths ($0.1R$ and $0.37R$, respectively). In the interior of a realistic red giant, the transition layer between the completely radiative zone and the convection zone extends much deeper than $0.1R$. The small humps at $z \approx 0.9$ correspond to the upper convective boundaries. The wiggles near $z \approx 0.1$ in (a) may be caused by the lower resolution of the numerical simulation.

unstable convective region, we estimate c_3 inside the convection zone. The values are approximately between 1 and 3. In the lower overshooting layer of Case I3, the value of $w'_z/(w'_x{}^2 + w'_y{}^2)$ stays around 0.6. This is not compatible with the prediction of Deng et al.

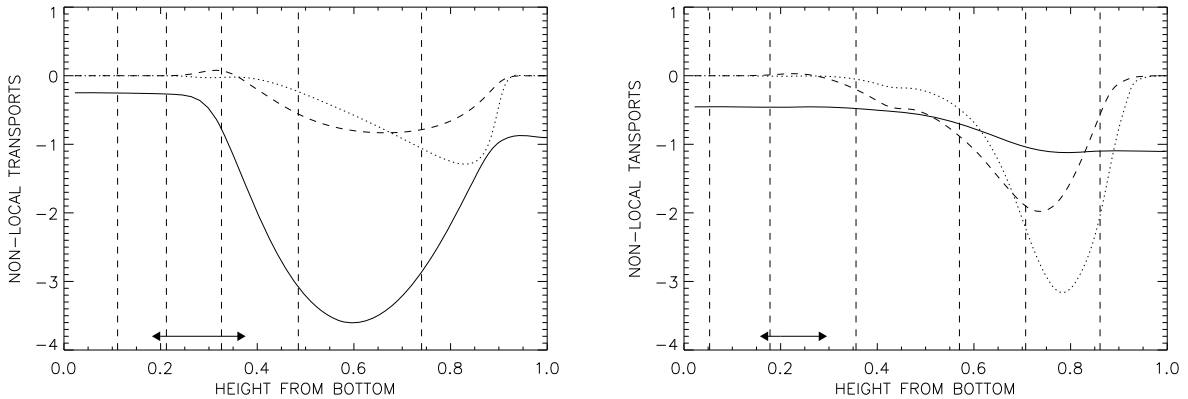


Figure 12. Some non-local turbulent transport coefficients for Cases I2 and M1. Left panel: Case I2. Solid line: $NLT1 \times 100$; dotted line: $NLT2 \times 1000$; dashed line: $NLT3 \times 100$. Right panel: Case M1. Solid line: $NLT1 \times 10$; dotted line: $NLT2 \times 50000$; dashed line: $NLT3 \times 1000$. The double-headed arrow indicates the overshooting zone.

(2006). This could be caused by the small size of the computed domain.

The anisotropy factor plays an important role in controlling the total amount of acoustic energy injected into the solar oscillation modes. For incompressible flows, the anisotropy factor adopted by Gough (1977) can be computed as $w'_z/(w'_x{}^2 + w'_y{}^2) = 1/(\Phi - 1)$. In Gough’s MLT, $\Phi = 1.3745$ can match the observed solar damping rates. On the other hand, Böhm-Vitense’s (1958) MLT requires $\Phi = 2$, which is close to the simulation results of Stein & Nordlund (1998). Our results show that in the region where the fluctuation of density is small, Φ is also very close to 2. It is therefore possible to derive theoretical values for Φ , such as $\Phi = 5/3$ for maximizing the convective heat flux (Gough 1978).

3.6 Correlation coefficients

It is instructive to compare the numerical results with those obtained by the 1D method of Xiong. Fig. 11 compares the correlation coefficients for the velocity and temperature fluctuations obtained by the different methods. Numerical simulations give more extensive overshooting and lower values of correlation in the convection zone. The larger overshooting may be caused by the large kinetic energy flux; this is negligible in Xiong’s theory. The extended distributions of the kinetic flux need to be balanced by similarly extended enthalpy fluxes. The temperature–velocity correlation is proportional to the enthalpy flux. Inside the convection zone, the numerical values of the correlation coefficient are close to that given in CS89 (0.81).

3.7 Non-local transport

In Xiong’s statistical turbulent convection theory, the non-local transport is assumed to be of the gradient type (Xiong 1989a; Xiong, Cheng & Deng 1998):

$$NLT1 = \overline{u'_k w'_i w'^i} = -\chi l_1 \nabla_k \overline{w'_i w'^i}, \quad (20)$$

$$NLT2 = \overline{u'_k \tilde{T}'^2 / \tilde{T}^2} = -\chi l_3 \nabla_k \left(\overline{\tilde{T}'^2 / \tilde{T}^2} \right), \quad (21)$$

$$NLT3 = \overline{u'_k \tilde{T}' / \tilde{T}} = -\chi l_5 \nabla_k \left(\overline{w'^i \tilde{T}' / \tilde{T}} \right), \quad (22)$$

with $l_1 \simeq l_3 \simeq l_5 = \Lambda$, where Λ is the Lagrangian integral length-scale of turbulence. The parameters introduced here, i.e. l_1, l_3 and

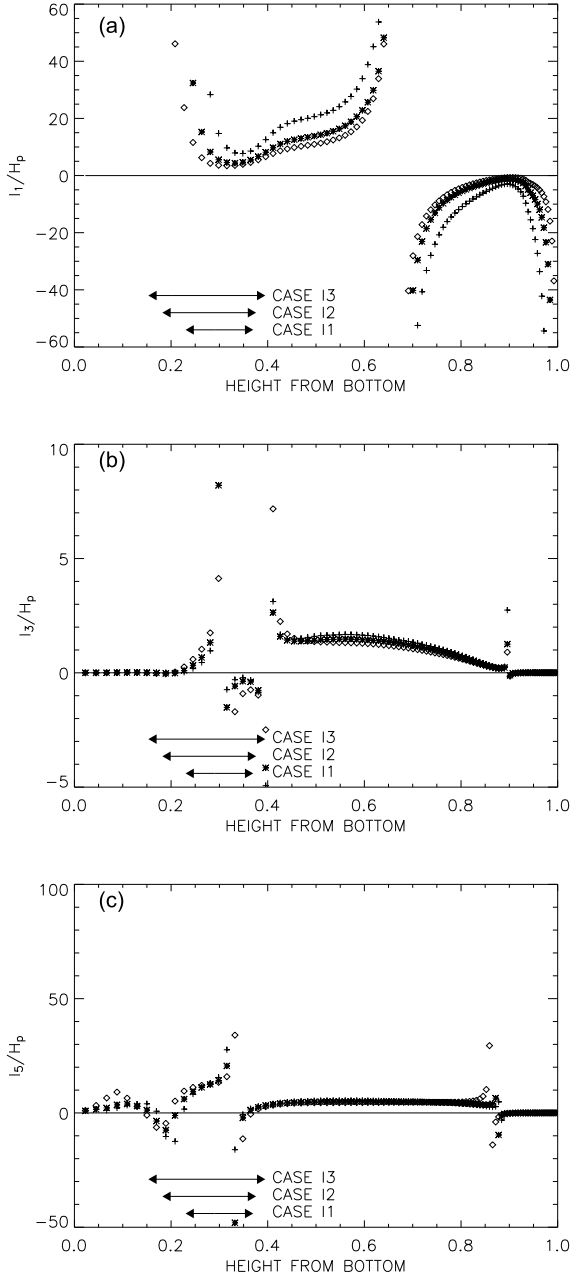


Figure 13. Non-local transport parameters for intermediate-mass star models. Plus symbols: Case I1; diamonds: Case I2; asterisks: Case I3. The double-headed arrows indicate the overshooting zone. The discontinuities in these height distributions are caused by either singularity or numerical errors. The values near these discontinuities are unreliable.

l_5 , are linked with c_2 and can be made dimensionless with H_p . The numerically obtained values of these non-local transport coefficients in Cases I2 and M1 are given in Fig. 12.

Estimations of l_1/H_p , l_3/H_p and l_5/H_p based on equations (20)–(22) are shown in Figs 13 and 14. There are no universal values for these parameters. The worst case is the gradient of turbulent kinetic energy: l_1/H_p is far from a constant. l_3/H_p is better and has a value around 1.5 in the unstable zone. It turns negative in the overshooting layer. l_5/H_p is roughly 5 in the unstable zone and of the order of 10 in the overshooting zone. These parameters seem independent of the details of the numerical models, since they have nearly the same profiles and magnitudes across Cases I1, I2 and I3. In the rapidly

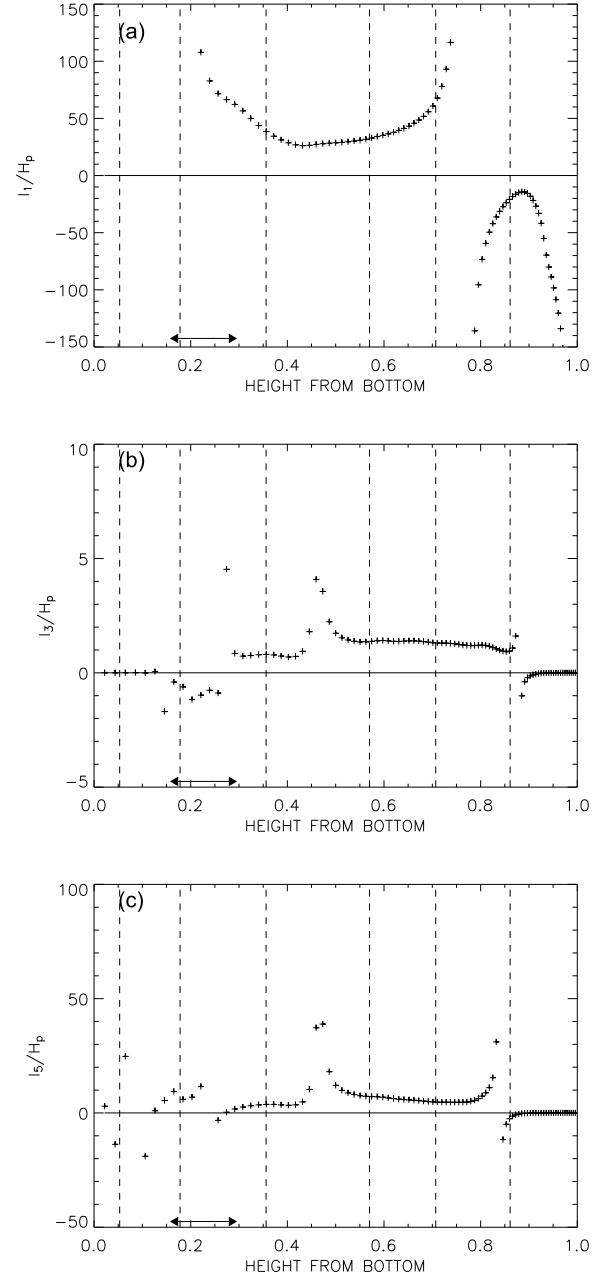


Figure 14. Non-local transport parameters for a massive star model. The double-headed arrow indicates the overshooting zone. The discontinuities are induced by the factors mentioned in the caption of Fig. 13.

varying region, the gradient approximations are too imprecise to be acceptable.

4 SUMMARY AND CONCLUSIONS

In this paper, we have presented three-dimensional numerical simulations of downward overshooting in the envelopes of massive and intermediate-mass giants. For the massive giant case, a 1D stellar model of a $15-M_\odot$ star was used as the initial model, while for the intermediate-mass giant case a $3-M_\odot$ star was mimicked qualitatively. In our simulations, we adopted an artificially modified OPAL opacity and treated radiative energy transport by the diffusion approximation. The gas was regarded as fully ionized and the radiation was included in the EOS. In order to reduce

the thermodynamic relaxation time-scale, the input energy fluxes of the intermediate-mass star models were enlarged by enhancing the radiative conductivity. A parametric investigation of such enhancement has been conducted. By statistical analysis of the thermodynamically relaxed state, the properties of overshooting below the convection zone were parametrized and compared with the 1D stellar model based on Xiong's non-local time-dependent turbulent convection theory. The main results are summarized as follows.

(i) The relative fluctuations of thermodynamical variables such as density, pressure and temperature are scaled by $F_b^{0.5}$, e.g. $T''/\bar{T} \propto F_b^{0.5}$, and the velocity fluctuations are scaled by $F_b^{0.25}$. These are different from the results based on simulations of efficient convection, which gave $T''/\bar{T} \propto F_b^{2/3}$ and $v_z'' \propto F_b^{1/3}$. The difference should be caused by the significant presence of radiation energy transfer. Since the amplification factor a_f is very large ($\sim 10^4$), the scaling relationships obtained here are preliminary and need to be investigated further.

(ii) Even though the convective regions in our models are quite shallow, the overshoot region is quite substantial ($\sim 1-2$ PSHs). In the lower overshooting zone the temperature gradient is superradiative.

(iii) The scaling relations between penetration distance, input flux and vertical velocity, e.g. $\Delta_c \propto F_b^{1/2}$, $\Delta_c \propto v_{z0}^{3/2}$, are acceptable in fitting current numerical results but may not be applicable to the actual modelling of intermediate-mass giants.

(iv) In the unstable region, the anisotropy ratio varies approximately between 1 and 3.

(v) The non-local turbulent transport is not well described by gradient models. No universal constant scaling parameters exist in both the unstable and overshooting zones.

It should be emphasized that the resolution and aspect ratio of our numerical experiments are limited by the computational resources. For intermediate-mass star models, the radial dimension (in PSHs) of the unstable region cannot cover the whole convection zone. The effects of enhanced resolution and greater depth need to be considered in future studies.

ACKNOWLEDGMENTS

We thank the Department of Astronomy at Peking University for providing computer time on their SGI Altix 330 system, on which the initial models were tested. We are also pleased to acknowledge use of computer time provided by X. P. Wu and the invaluable contributions of D. R. Xiong to the current research. This work was partially supported by the Chinese National Natural Science Foundation (CNNSF) through Grant No. 10573022. KLC thanks Hong Kong RGC for support (project no. 600306).

REFERENCES

Baker N. H., 1987, in Hillebrandt W., Meyer-Hofmeister E., Thomas H.-C., eds, *Physical Processes in Comets, Stars, and Active Galaxies*. Springer, Berlin, p. 105

Basu S., Antia H. M., Narasimha D., 1994, *MNRAS*, 267, 209
 Böhm-Vitense E., 1958, *Astrophysik*, 46, 108
 Brummell N. H., Clune T. L., Toomre J., 2002, *ApJ*, 570, 825
 Canuto V. M., 1993, *ApJ*, 416, 331
 Chan K. L., Sofia S., 1986, *ApJ*, 307, 222
 Chan K. L., Sofia S., 1989, *ApJ*, 336, 1022 (CS89)
 Chan K. L., Sofia S., 1996, *ApJ*, 466, 372
 Chan K. L., Wolff C. L., 1982, *J. Comput. Phys.*, 47, 109
 Deng L. C., Xiong D. R., Chan K. L., 2006, *ApJ*, 643, 426
 Deng L. C., Xiong D. R., 2008, *MNRAS*, 386, 1979
 Emden R., 1907, *Gaskugeln*. Teubner, Leipzig
 Gough D. O., 1977, *ApJ*, 214, 196
 Gough D. O., 1978, in Belvedere G., Paterno L., eds, *Proc. ESP Workshop on Solar Rotation*. Catania Univ. Press, Catania, p. 337
 Graham E., 1975, *J. Fluid Mech.*, 70, 689
 Keller L. V., Friedmann A., 1924, in Biezeno C. B., Burgers J. M., eds, *Proc. First International Congress on Applied Mechanics*. J. Waltman Jr, Delft, p. 395
 Kim Y. C., Chan K. L., 1998, *ApJ*, 496, L121
 Malagoli A., Cattaneo F., Brummell N. H., 1990, *ApJ*, 361, L33
 Pal P. S., Singh H. P., Chan K. L., Srivastava M. P., 2007, *Ap&SS*, 307, 399
 Porter D. H., Woodward P. R., 2000, *ApJS*, 127, 159
 Richtmyer R. D., Morton K. W., 1968, *Difference method for initial value problems*. Interscience, New York
 Rogers F. J., Iglesias C. A., 1992, *ApJS*, 79, 507
 Rogers F. J., Swenson F. J., Iglesias C. A., 1996, *ApJ*, 456, 902
 Rogers T. M., Glatzmaier G. A., Jones C. A., 2006, *ApJ*, 653, 765
 Roxburgh I. W., 1998, in Chan K. L., Cheng K. S., Singh H. P., eds, *ASP Conf. Ser. Vol. 138, Proc. 1997 Pacific Rim Conf. on Stellar Astrophysics*. Astron. Soc. Pac., San Francisco, p. 411
 Roxburgh I. W., Simmons J., 1993, *A&A*, 277, 93
 Saikia E., Singh H. P., Chan K. L., Roxburgh I. W., Srivastava M. P., 2000, *ApJ*, 529, 402
 Schmitt J. H., Rosner R., Bohn H. U., 1984, *ApJ*, 282, 316
 Singh H. P., Roxburgh I. W., Chan K. L., 1994, *A&A*, 281, L73
 Singh H. P., Roxburgh I. W., Chan K. L., 1995, *A&A*, 295, 703
 Singh H. P., Roxburgh I. W., Chan K. L., 1998, *A&A*, 340, 178
 Spiegel E. A., 1971, *ARA&A*, 9, 323
 Stein R. F., Nordlund Å., 1989, *ApJ*, 342, L95
 Stein R. F., Nordlund Å., 1998, *ApJ*, 499, 914
 Tian C. L., Deng L. C., Chan K. L., Xiong D. R., 2009, *Res. Astron. Astrophys.*, 9, 102 (TDXC)
 Xiong D. R., 1977, *Acta Astron. Sinica*, 18, 86
 Xiong D. R., 1985a, *Sci. Sinica*, 28, 764
 Xiong D. R., 1985b, *A&A*, 150, 133
 Xiong D. R., 1986, *A&A*, 167, 239
 Xiong D. R., 1989a, *A&A*, 209, 126
 Xiong D. R., 1989b, *A&A*, 213, 176
 Xiong D. R., Cheng Q. L., Deng L. C., 1998, *ApJ*, 500, 449
 Xiong D. R., Deng L. C., 2001, *MNRAS*, 327, 1137 (XD2001)
 Zahn J.-P., 1991, *A&A*, 252, 179

This paper has been typeset from a $\text{\TeX}/\text{\LaTeX}$ file prepared by the author.